Multi-scale interactions in an idealized Walker cell: Simulations with sparse space-time superparameterization

Joanna Slawinska

Olivier Pauluis

Andrew Majda

Wojciech W. Grabowski

Courant Institute of Mathematical Sciences, New York University, New York, NY

National Center for Atmospheric Research, Boulder, CO

ABSTRACT

This paper discusses the Sparse Space and Time SuperParameterization (SSTSP) algorithm and evaluates its ability to represent interactions between moist convection and the large-scale circulation in the context of a Walker cell flow over a planetary scale two-dimensional domain. The SSTSP represents convective motions in each column of the large-scale model by embedding a cloud-resolving model, and relies on a sparse sampling in both space and time to reduce computational cost of explicit simulation of convective processes. Simulations are performed varying the spatial compression and/or temporal acceleration, and results are compared to the cloud-resolving simulation reported previously. The algorithm is able to reproduce broad range of circulation features for all temporal accelerations and spatial compressions, but significant biases are identified. Precipitation tends to be too intense and too localized over warm waters when compared to the cloud-resolving simulations. It is argued that this is because coherent propagation of organized convective systems from one large-scale model column to another is difficult when superparameterization is used, as noted in previous studies. The Walker cell in all simulations exhibits low-frequency variability on time scale of about 20 days, characterized by 4 distinctive stages: suppressed, intensification, active, and weakening. The SSTSP algorithm captures spatial structure and temporal evolution of the variability. This reinforces the confidence that SSTSP preserves fundamental interactions between convection and the large-scale flow, and offers a computationally efficient alternative to traditional convective parameterizations.

1. Introduction

The interplay between moist convection and the large-scale flow is the fundamental feature of the tropical atmosphere. However, the extreme range of spatial and temporal scales involved makes it difficult to resolve all relevant processes in numerical models. In large-scale models, this issue has traditionally been addressed through the use of convective parameterizations that account for effects of convective motions on the mean atmospheric temperature and humidity profiles. It is well recognized, however, that convective parameterizations fail to reproduce many important features of the tropical atmosphere. This is partly because many aspects of convection, such as downdrafts, cold pools, and mesoscale organization, are either excluded or poorly represented in the parameterizations. Moreover, the parameterizations often do not reproduce the intrinsic intermittency of moist convection. This motivates the development of new approaches to improve the representation of convection in multi-scale simulations of the tropical atmosphere.

One way to improve such simulations is to take advantage of cloud-resolving modeling. Cloud models emerged in 1970s (e.g., Steiner 1973; Schlesinger 1975; Klemp and Wilhelmson 1978; Clark 1979) to study individual clouds in short simulations (tens of minutes) and typically applied idealized forcing techniques (e.g., initiating cloud development via a warm bubble). More recently such models have been used in significantly longer simulations (days and weeks) and applying large computational domains. Such simulations are often driven by observationally-based time-evolving larger-scale forcings and allow better comparisons with observations (e.g., Grabowski et al. 1996, 1998; Xue and Randall 1996; Xue et al. 2002, Fridlind et al. 2012, among many others). Cloud-resolving models solve non-hydrostatic governing equations and allow convective development in conditionally unstable conditions. The horizontal resolution of $\sim$1 km is high enough for the simulation of dynamical evolution of individual clouds, with microphysical, turbulent and radiative processes needed to be parameterized. Explicit representation of cloud dynamics allows capturing key features that convective parameterizations struggle with. During the last 30 years, many studies focused on statistical response of cloud ensembles to the large-scale forcing over a limited area (e.g., Soong and Ogura 1980, Soong and Tao 1980, Tao and Soong 1986). So far, cloud-resolving models appear superior to any kind of convective parameterization, as found by comparing model results to observations. However, the computational cost still severly limits global cloud-resolving simulations and alternative approaches need to be explored. An important application of cloud-resolving modeling in the context of global simulation is validation and improvement of other approaches designed to estimate feedbacks from convective to mesoscale, synoptic and global scales.

Rescaling approaches have also been suggested to extend cloud-resolving modeling to global simulations. The underlying idea is to artificially reduce the scale separation between convective and planetary scales, and thus to make explicit simulation of convection computationally feasible in global domains. The Diabatic Acceleration and Rescaling (DARE) approach (Kuang et al. 2005) and the hypo-hydrostatic approach (Pauluis et al. 2005, Garner et al. 2005) are examples of such techniques. In DARE, the Earth's diameter is reduced, the rotation rate is increased, and diabatic processes are accelerated. In the hypo-hydrostatic approach, the vertical acceleration is rescaled. Pauluis et al. (2005) have shown that both approaches are mathematically equivalent and they reduce the scale separation between convection and the planetary scale without affecting the dynamics at large scales. However, changes in the behavior of convection due to the rescaling limit the applicability of these methods. Nevertheless, they illustrate how mathematical rescaling can offer a computationally efficient way to use cloud-resolving models in global simulations.

The second approach is to take advantage of a cloud-resolving model for global simulations through the superparameterization methodology (Grabowski and Smolarkiewicz 1999; Grabowski 2001, 2004; Randall et al. 2001). In this framework, a two-dimensional cloud-resolving model with periodic lateral boundaries is embedded within each column of a global model to simulate interactions between convective and global scales. The simulated large-scale scale flow includes the convective feedback from small to large scales, and convective scales respond to the forcing from the large-scale dynamics. In the original superparameterization (SP thereafter), convective feedback is calculated using a cloud-resolving model applying horizontal domain equal (or approximately equal) to the large-scale model horizontal gridlength. Grabowski (2001, section 3) simulated a 2D Walker cell of 4000 km horizontal extent applying SP approach with different horizontal gridlengths (from 20 to 500 km) and thus different extents of the SP model horizontal domain. Results from these simulations were compared to the fully-resolved simulations (described in Grabowski et al. 2000) as well as between each other. SP seemed reasonably successful in reproducing large-scale conditions as simulated by the cloud-resolving model (e.g., dry subsidence and humid ascent regions, large-scale flow featuring the first and second baroclinic modes, etc.). However, mesoscale organization of convection and the strength of the quasi-two-day oscillations, the prominent feature of the fully-resolved simulations, were significantly different between SP simulations.

Over the last ten years, SP has been tested in many studies of tropical dynamics. Khairoutdinov et al. (2005) and DeMott et al. (2007) found that while Madden Julian Oscillation (MJO) is missing from the standard Community Atmosphere Model (CAM), it is simulated reasonably well with SP-CAM (i.e., the superparameterized CAM). They report several important improvements in simulating tropical climatology, such as a more realistic distribution of cirrus cloudiness or intense precipitation. However, some important biases persist, for instance, too heavy precipitation over the western tropical Pacific associated with the Indian monsoon or too low shallow-convection cloud fraction and light rain across parts of the tropics and subtropics. Studies attempting to explain the reason of excessive precipitation in western Pacific during monsoon periods typically find significant correlation between moisture content in the column and precipitation. Thayer-Calder and Randall (2009) suggest that the difference comes from contrasting profiles of convective heating that excite different large-scale circulation (and thus affect surface wind and evaporative feedback) and subsequently differently moisten the troposphere. Luo and Stephens (2006) argue that convection-evaporation feedback is the main culprit of excessive rain and suggest that this may be due to the periodicity of SP's cloud-resolving models leading to the prolonged presence of precipitating convection at a given location.

The mathematical aspects of the SP implementation are important as illustrated by the above examples and other studies (e.g., Grabowski 2004). Over the years, several algorithms have been proposed to implement the SP framework. Here, we evaluate the ability of the Sparse Space and Time SuperParameterization (SSTSP) to accurately reproduce the interactions between convection and the large-scale flow. In the SSTSP framework, described in more detail in the next section, the embedded cloud-resolving model applies horizontal domain that is small in comparison to the horizontal gridlength of the large-scale model, and for the time period that is short when compared to the time step of the large-scale model. SSTSP combines the spatial compression used in the previous SP implementation (Xing et al. 2009) with a temporal acceleration similar to the DARE and hypo-hydrostatic rescaling, thus significantly increasing computational efficiency of the approach. As with the original SP, the goal of SSTSP algorithm is to obtain statistically correct representation of the convective impact on the large-scale flow at reduced computational cost.

Preliminary SSTSP testing reported in Xing et al. (2009) applied two-dimensional simulations of an idealized squall line propagating in a periodic horizontal domain of 1024 km. Performance of SSTSP algorithm was examined for a range of environmental conditions that differed in the prescribed vertical shear of the large-scale horizontal wind. SSTSP algorithm seemed to capture propagation of the squall line and its speed. In particular, propagation speed appeared to be strongly controlled by vertical profile of the large-scale shear, with no significant drawbacks of the SSTSP algorithm. Contrasting convective organizations were simulated for different shears, from squall line to decaying convection. This provided hope for the SSTSP algorithm in simulations of different convective regimes for various large-scale conditions. Furthermore, structural agreement was found for large-scale features of simulated convective systems since pattern correlation was high for horizontal velocity or specific humidity. However, the impact of SSTSP algorithm on large-scale features (e.g., the mean temperature and moisture profiles) was severely limited because of the short simulation time (36 hours) and relatively small computational domain.

Here, we investigate the accuracy of the SSTSP algorithm in reproducing interactions between convection and the large-scale flow in an idealized Walker cell circulation. We compare SSTSP results against the benchmark solution obtained with the cloud-resolving model. The latter is described in more detail in Slawinska et al. (2014; SPMG hereinafter) focusing on the intra-seasonal variability of the Walker cell with the time-scale of about 20 days. The low-frequency oscillation features four phases: the suppressed, intensification, active, and weakening. Intensification of the circulation is associated with the broadening of the large-scale ascent region, which in turn is strongly coupled to propagating synoptic-scale systems. Details of the SSTSP framework and its implementation are given in section 2. Results of simulations applying the SSTSP framework are discussed in section 3 and compared to the results from SPMG's cloud-resolving model. Section 4 provides a discussion of model results and concludes the paper.

2. Model and experimental setup

In this study, we use the anelastic nonhydrostatic atmospheric model EULAG (Smolarkiewicz and Margolin 1997; see Prusa et al. 2008 for a comprehensive review) applying the SP methodology (Grabowski 2001; 2004) and implement the SSTSP framework as described briefly below (see also Xing et al. 2009).

a. *SP and SSTSP frameworks*

1) Large-scale and cloud-resolving model equations

The large-scale and cloud-resolving models calculate evolution of the large-scale Φ and small-scale φ variables:

$$\Phi = [U, W, \Theta, Q_v, Q_c, Q_p], \tag{1}$$

$$\varphi = [u, w, \theta, q_v, q_c, q_p]. \tag{2}$$

The variables are the horizontal (U and u) and vertical (W and w) velocities, potential temperature (Θ and θ), water vapor (Q_v and q_v), condensed water/ice (Q_c and q_c), and precipitating water/ice (Q_p and q_p) mixing ratios, the latter two following representation of moist thermodynamics of Grabowski (1998). Evolution of Φ and φ can be symbolically written as:

$$\frac{\partial \Phi}{\partial t} + A_\Phi = S_\Phi + F_\Phi^{CS} \tag{3}$$

$$\frac{\partial \varphi}{\partial t} + A_\varphi = S_\varphi + F_\varphi^{LS} \tag{4}$$

where $A_\Phi \equiv \frac{1}{\rho_o}\frac{\partial}{\partial X_j}(\rho_o U_j \Phi)$ and $A_\varphi \equiv \frac{1}{\rho_o}\frac{\partial}{\partial x_j}(\rho_o u_j \varphi)$ represent the large-scale and small-scale advection terms, respectively; S_Φ and S_φ represent various source terms in the large-scale and small-scale models (such as the buoyancy, pressure gradient, radiative cooling, surface fluxes, phase changes of the water substance, precipitation formation and fallout, gravity wave absorber, etc.); F_Φ^{CS} is the small-scale feedback; and F_φ^{LS} stands for the large-scale forcing. The latter two terms represent the coupling between the two models. The source terms S_Φ and S_φ need to be appropriately designed between the two models. For instance, the pressure gradient terms are independently formulated between the models (e.g., via the anelastic continuity equation). The horizontally-averaged vertical velocity at each level of the small-scale model has to vanish because of the periodic lateral boundary conditions, and the vertical velocity field cannot be coupled between the two models. Surface fluxes, radiative transfer, phase changes and precipitation formation/fallout are typically considered in the small-scale model only and they affect the large-scale fields through the small-scale feedback. In general, one needs to ensure that a given source is included only once between the two models, that is, no double-counting takes place.

2) Coupling procedure in SP

The original implementation of the SP is as follows (cf. Grabowski 2004). Every large-scale grid, $\Delta X \times \Delta Z$, contains a cloud-resolving (small-scale) model that has $N_x \times N_z$ grid points of grid size $\Delta x \times \Delta z$, for which

$$\Delta X = N_x \Delta x; \Delta Z = \Delta z, \tag{5}$$

that is, the horizontal extent of the small-scale model domain is equal to the horizontal gridlength of the large-scale model, and the two models share the same vertical grid. For a given large-scale time step, ΔT, the evolution from time T to $T + \Delta T$ of the large-scale variable is calculated first:

$$\Phi|^{T+\Delta T} = \Phi|^{T} + \Delta T (A_\Phi + S_\Phi)|_T^{T+\Delta T} + \Delta T F_\Phi^{CS}|^T, \tag{6}$$

with $\Delta T (A_\Phi + S_\Phi)|_T^{T+\Delta T}$ standing for the transport and large-scale sources over the period $(T : T + \Delta T)$ and $F_\Phi^{CS}|^T$ representing the small-scale feedback calculated at previous time, T, as given by Equation (10).

With the large-scale variables already known at $(T + \Delta T)$ the vertical profiles of large-scale forcing for the small-scale variables, $F_\varphi^{LS}|^T$, are formulated as follows:

$$F_\varphi^{LS}|^T = \frac{\Phi|^{T+\Delta T} - < \varphi|^T > |_1^{N_x}}{\Delta T}, \tag{7}$$

where $< . > |_1^{N_x}$ stands for the horizontal averaging over the N_x points of the small-scale model. With the large-scale forcing formulated as above and assumed constant for the large-scale time step, the small-scale model equations are advanced from T to $T + \Delta T$:

$$\varphi|^{T+\Delta T} = \varphi|^{T} + \sum_{i=1}^{N_t} \Delta t (A_\varphi + S_\varphi)|_{T+(i-1)\Delta t}^{T+i\Delta t} + \sum_{i=1}^{N_t} \Delta t F_\varphi^{LS}|^T, \tag{8}$$

over N_t time steps for which:

$$\Delta T = N_t \Delta t. \tag{9}$$

Finally, at the end of the large-scale model time step, average profiles of the small-scale feedback are formulated as:

$$F_{\Phi}^{CS}|^{T+\Delta T} = \frac{< \varphi|^{T+\Delta T} > |_1^{N_x} - \Phi|^{T+\Delta T}}{\Delta T}. \tag{10}$$

Repeating (8), (9), (10), and (12) allows stepping forward in time of the combined small-scale and large-scale system.

3) Sparse space-time algorithm

The sparse space-time algorithm (Xing et al. 2009) reduces the computational cost of the SP by decreasing the horizontal extent of small-scale domain by a factor of p_x (i.e., p_x smaller number of model columns; reduced space strategy) and the number of small-scale time steps by a factor of p_t (reduced time strategy). In such a case, the number of small-scale time steps in every large-scale time step and the number of columns in every large-scale grid, N_{p_t} and N_{p_x}, are given by:

$$N_{p_t} = \frac{N_t}{p_t}, \tag{11}$$

$$N_{p_x} = \frac{N_x}{p_x}. \tag{12}$$

As in the original SP, the evolution of the large-scale variables is calculated first according to (6). Then, profiles of the large-scale forcings are calculated for the small-scale domain of N_{p_x} horizontal columns similarly to (9):

$$F_{\varphi}^{LS}|^{T} = p_t \frac{\Phi|^{T+\Delta T} - < \varphi|^{T} > |_1^{N_{px}}}{\Delta T}, \tag{13}$$

but including p_t (i.e., adding the time rescaling of the large-scale forcing), and applying horizontal averaging over the rescaled small-scale domain (marked $< . > |_1^{N_{px}}$). Subsequently, accelerated evolution of the small-scale variables over N_{p_t} time steps are calculated similarly to (10):

$$\varphi|^{T+\frac{\Delta T}{p_t}} = \varphi|^{T} + \sum_{i=1}^{N_{p_t}} \Delta t (A_\varphi + S_\varphi)|_{T+(i-1)\Delta t}^{T+i\Delta t} + \sum_{i=1}^{N_{p_t}} \Delta t F_\varphi^{LS}|^{T}. \tag{14}$$

The small-scale variables at the end of the large-scale time step, $\varphi|^{T+\Delta T}$, are assumed equal to the solution of (17) with accelerated forcing, that is,:

$$\varphi|^{T+\Delta T} = \varphi|^{T+\frac{\Delta T}{p_t}}. \tag{15}$$

Finally, profiles of the small-scale feedback are computed as:

$$F_\varphi^{CS}|^{T+\Delta T} = \frac{\varphi|^{T+\frac{\Delta T}{p_t}} - \Phi|^{T+\Delta T}}{\Delta T}. \tag{16}$$

Elementary considerations (similar to those involving Eqs. 10 and 11 in Grabowski 2004) document that the SSTSP algorithm outlined above ensures appropriate transfer of information between the small-scale and large-scale models despite spatial compression and temporal acceleration. For instance, if either S_Φ in (3) or S_φ in (4) is assumed constant, then the tendency due to this source is correctly passed from one model to another (i.e., from the large-scale to small-scale model for S_Φ and vice-versa for S_φ) when spatial compression and temporal acceleration are applied.

Beyond mathematical consistency, one should be also aware of physical limitations of the SSTSP methodology. For the spatial compression, small horizontal domain of the small-scale model may affect not only the statistical sampling of small-scale features, but their evolution as well, evolution of convective cells in particular. Since the mean vertical velocity within SP models at any level has to vanish (because of periodic lateral boundary conditions), the upward convective mass flux has to be balanced by the environmental subsidence. The key point is that the vertical development of convective clouds may be affected when the computational domain is reduced to a small number columns. The temporal acceleration is perhaps more difficult to interpret. The approach taken in Xing et al. (2009) and followed here (cf. Eq. 16) implies that the large-scale forcing is increased in proportion to the temporal acceleration factor p_t. The idea is that the original large-scale forcing has to be increased so the small-scale processes can appropriately respond over the p_t-shorter time. An alternative approach might be to keep the large-scale forcing unchanged, but instead increase the small-scale feedback by p_t. In other words, the small-scale response to the original feedback would be calculated only for the p_t-fraction of ΔT and linearly extrapolated (i.e., increased by a factor of p_t) before applied to the large-scale model. Such a procedure would lead to the same evolution in time of Ψ and φ for the case of a constant source. However, considering fundamental differences between time scales involved in small-scale and large-scale processes, extrapolation of the small-scale response seems more problematic than scaling up the large-scale forcing.

b. Experimental design

Developments presented in the previous section are tested applying the Walker cell circulation in the two-dimensional domain following SPMG. As in SPMG, the environmental profiles come from a simulation of radiative-convective equilibrium applying a cloud-resolving model SAM with NCAR CAM3 interactive radiation scheme (Khairoutdinov and Randall 2003). The planetary-scale circulation is driven by the surface fluxes and radiative cooling. The sea surface temperature (SST) distribution is given by a cosine squared function, with 303.15 K in the center and 299.15 K at the periodic lateral boundaries. Radiative cooling is given by the average profile of radiative tendency in the radiative-convective simulation and by the relaxation term towards the equilibrium value of potential temperature with the 20-day timescale. More detailed description of the modeling setup can be found in SPMG which discusses results from the cloud-resolving simulation that provide the reference for SP simulations.

In SP simulations, the large-scale domain spans 40,000 km with horizontal and vertical gridlengths of 48 km and 500 m, respectively. The large-scale time step is 180 s. The cloud-resolving domain has horizontal and vertical gridlengths of 2 km and 500 m, respectively, and the small-scale time step of 15 s. The simulations are run for 340 days, and the last 290 days are analyzed. Because of the simulation length, no other SP setups (i.e., either larger or smaller large-scale model gridlength, cf. section 3 of Grabowski 2001) were considered. Simulations with various time accelerations and space compressions are compared. Horizontal domain of the cloud-resolving model is equal to the large-scale horizontal gridlength (i.e., $p_x = 1$) or is reduced by a factor of 2 ($p_x = 2$) or 3 ($p_x = 3$). Also, for every large-scale time step, time integration in cloud-resolving domains is performed for the period either equal ($p_t = 1$) or two ($p_t = 2$), three ($p_t = 3$) and four ($p_t = 4$) times shorter than the large-scale model time step. A simulation with a given spatial compression (p_x) and temporal acceleration (p_t) will be referred to as "SSTSP$p_x p_t$ simulation". For instance, a simulation with $p_x = 2$ and $p_t = 3$ will be called "SSTSP23 simulation". In total, 12 simulations are performed with different time accelerations and space compressions. We will refer to them as "SSTSP simulations". SSTSP simulations are compared to the benchmark case obtained with the cloud-resolving model and analyzed in SPMG, and refereed to as the "CRM simulation" thereafter.

3. Results

SSTSP simulations reproduce the key characteristics of the CRM simulation. In particular, large-scale overturning circulation is simulated in the large-scale domain, with the large-scale ascent over warm pool and subsidence over cold SSTs. Similarly to the CRM simulation, variability across wide range of scales is simulated. We start with a discussion of the mean state. Subsequently, we present analysis of high- and low-frequency variability, with the latter analyzed in more detail. The emphasis is on comparing the SP and CRM simulations (the latter one documented in details in Slawinska et. al. (2014)) and evaluating the impact of the spatial and temporal scaling factors p_x and p_t.

a. *The mean Walker cell circulation*

Figure 1 shows the time-averaged horizontal velocity field for the CRM and SSTSP simulations (the former already shown in Fig. 2a in SPMG) as well as the difference between them. The CRM large-scale circulation features surface and mid-tropospheric mean horizontal flows towards the highest SST in the center of the domain. The horizontal velocity maxima are around 10 and 5 $\mathrm{m\,s^{-1}}$ at the surface and around 6-km altitude, respectively. The upper-tropospheric outflow from the center of the domain features maximum velocities of over 20 $\mathrm{m\,s^{-1}}$. SSTSP simulations exhibit similar large-scale circulations, with low- and mid-level convergence accompanied by the upper-tropospheric divergence over warm SSTs, that is, with the first and second baroclinic modes. The most apparent difference between CRM and SSTSP simulations is the narrower ascending region in the center of the domain in SSTSP cases. Although the patterns and amplitudes of the horizontal flow are similar in all simulations, the difference plots between CRM and SSTSP show significant deviations that seem to increase with the spatial compression and temporal acceleration, with the SP simulation without compression and acceleration (i.e., SSTSP11) being the closest to CRM as one might expect. Although not shown in the figure, the differences depend primarily on the horizontal extent of the SP domains (i.e., they increase with the increase of p_x), and there seems to be no systematic impact of the temporal acceleration (i.e., increasing the p_t parameter).

Figure 2 and 3 document the impact of spatial compression and time acceleration on the mean (i.e., horizontal- and time-averaged) profiles of the potential temperature and water vapor mixing ratio. Figure 2 shows the difference between profiles from SSTSP with various spatial compressions and CRM. Mean profiles for the SSTSP11 simulation are close to CRM, and the differences increase with the spatial compression. The SSTSP31 simulation features up 8 K colder upper troposphere and up to 2 g/kg lower moisture in the lower troposphere when compared to CRM. The relative humidity profiles (not shown) agree relatively well below 8 km for all simulations and differ significantly above 10 km, with no obvious sensitivity to the spatial compression. The differences between the temperature profiles are consistent with a heuristic argument that reducing the horizontal extent of SP computational domains (i.e., increasing p_x) makes convective overturning more difficult and leads to a colder upper troposphere. The water vapor difference profiles can be explained by a narrower ascending region in the center of the domain as illustrated in Fig. 1 and further quantified below. As shown in Fig. 3, time acceleration leads to the mean temperature/moisture profiles that are warmer/more humid, but the effects are significantly smaller than for the spatial compression, especially for the moisture.

Figure 4 and 5 show spatial distributions of the difference between the SSTSP and CRM simulations for the mean temperature and water vapor mixing ratio, respectively. The differences are averaged over days 50 to 340. For the temperature, the patterns are dominated by the differences in the mean profiles (cf. Fig. 2), with small gradients between regions with high and low SST (i.e., mean ascent and mean subsidence). In the CRM simulation, the temperature field at a given level is homogenized by convectively-generated gravity waves that maintain small horizontal temperature gradient. Such a mechanism is also efficient in SP simulations, including SSTSP, as documented by relatively small horizontal temperature gradients in Fig. 4. Water vapor field, on the other hand, can only be homogenized by the physical advection and the differences between SSTSP and CRM simulations are larger, as shown in Fig. 5. The largest differences (in the absolute sense) are near the center of the domain, likely because of the different width of the central ascending region and differences in the large-scale circulation (cf. Fig. 1). The differences increase with the increase of the spatial compression and temporal acceleration. The lower troposphere above 1 km is drier in SSTSP than in the CRM, and in both the ascent and subsidence regions, perhaps with the exception of the narrow zone over the coldest SSTs. The level of maximum difference outside the central region at heights between 2 and 3 km corresponds to the low level cloud tops (see below). Upper troposphere is drier at the warm pool edges, likely because of the narrower region of deep convection in the SSTSP simulations.

Figure 6 and 7 show time-averaged mean fields and profiles of the cloud condensate mixing ratio, respectively. Fig. 6 shows that shallow convection occurs over the entire domain, while deep convection is confined to the warm pool. The region with deep convection narrows when the spatial compression and temporal acceleration increase. There are also systematic changes of the mean cloud condensate profiles as documented in Fig. 7. The figure documents the classical trimodal characteristics of the tropical moist convection: shallow, congestus, and deep (cf. Johnson et al. 1999), with the lower-tropospheric maximum associated with shallow convective clouds, and middle- and upper-troposheric maxima marking detrainment levels from congestus and deep convection, respectively. Temporal acceleration results in a significant shift of the profiles towards higher values (factor of approximately 2 between panels a and d). Spatial compression for a given temporal acceleration has relatively smaller effect, with systematic decrease of cloud condensate above 5 km.

Figure 8 shows mass flux profiles for CRM and SSTSP simulations with various spatial compressions and temporal accelerations. Since these profiles are derived by averaging the cloud-model data, they represent the impact of the SSTSP methodology on convective transport. The SP simulation with neither spatial compression nor temporal acceleration (i.e., SSTSP11) gives the mean mass flux close to the one from the CRM simulation. Spatial compression (i.e., SSTSP31) leads to significantly reduced mass flux, arguably because of the impact of a reduced extent of the cloud-model computational domain on the convective transport as argued at the end of section 2a. In contrast, temporal acceleration (i.e., SSTSP13) leads to a significant increase of the mass flux, arguably because of the increase of the large-scale forcing (cf. Eqs. 7 and 13). Combining spatial compression and temporal acceleration (i.e., SSTSP33) results in the convective mass flux in between simulations with either spatial compression or temporal acceleration.

The differences in the convective mass flux affect the mean (domain and time averaged) profiles of the precipitation water mixing ratio as shown in Fig. 9. The simple microphysics parameterization used in the simulations assumes precipitation to be in the form of snow/rain in the upper/lower troposphere, with snow sedimenting with significantly smaller vertical velocity. This explains the difference between lower- and upper-tropospheric values of each profile. However, the magnitude of the profiles (i.e., the largest/smallest for SSTSP13/SSTSP31) is in direct response of the convective mass flux shown in Fig. 8. The difference between precipitation water profiles might have a significant impact on model results once an interactive radiation scheme is used in place of a prescribed radiative cooling applied in current simulations.

SSTSP framework significantly modifies the spatial distribution of convection and related statistics. The differences in cloudiness are associated with different spatial distributions of the time-averaged precipitable water content, cloud top temperature and precipitation rate, as shown in Figure 10, respectively, with their mean values given in Table 1. As the figures document, SSTSP simulations are characterized by significantly narrower distributions of all the quantities. In the CRM simulation, central 10,000 km is characterized by the mean cloud top temperature around 288 K, precipitable water around 75 kg m^{-2}, and surface precipitation around 0.45 mm hr^{-1}. All distributions are relatively flat and feature steep gradients at the edges of the warm pool with the mean precipitation dropping below 0.1 mm hr^{-1} and mean cloud top temperature increasing to around 300 K. SSSTP simulations, on the other hand, are characterized by narrow distributions, with peaks at the center and steep gradients of the mean cloud top temperature and precipitation. These differences also occur in SSTSP11, that is, the SP simulation with neither time acceleration nor spatial compression, and thus are a general feature of the SP simulation.

Because of the complicated impact of the time acceleration on diabatic processes, an intrinsic feature of the SSTSP framework, it is impossible to rescale the cloud top temperature between CRM and SSTSP simulations. Increasing temporal acceleration leads more intense convective activity (c.f., Fig. 8), increased cloudiness and precipitable water, and decreased mean cloud top temperature (c.f., Table 1). These aspects of temporal acceleration have been pointed out by Pauluis et al. (2005) and they seem related to the way microphysical processes (in particular fallout of rain) are handled. No acceleration of microphysical processes is applied here, potentially impacting the balance between processes responsible for moistening and drying the troposphere.

In summary, SSTSP framework appears to simulate 2D Walker circulation qualitatively well. In particular, mean large-scale flow consists of deep overturning circulation (first baroclinic mode) and mid-tropospheric jet (second baroclinic mode). Deep convection occurs primarily over the warm pool, and subsidence regions are dominated by shallow convection. However, detailed comparison reveals systematic differences in the model mean state. These differences are mainly artifacts of the original implementation of SP, without significant drawbacks of the SSTSP framework. The artificial scale separation between large-scale and small-scale models and periodicity of small-scale models impose significant limitations on the flow field in the small-scale domain (e.g., vanishing mean mass flux) and subsequently on the simulated convection and its organization. Convective feedback to large-scales and mean large conditions are modified accordingly.

b. Transients

SPMG document several transient features occurring in CRM simulation. The large-scale flow is characterized by low-frequency variability featuring 20-day oscillations with alternating periods of strong and weak overturning circulation. The strong circulation phase is associated with intense convection and expansion of the large-scale convergence region over the warmest SSTs. The weak circulation phase, on the other hand, features reduced convective activity and narrower convergence region. The expansion/compression of the convergence region coincides with synoptic-scale convective activity propagating from/to the centre of the domain with the average speed between 5 and 10 m s^{-1}.

Here, we investigate if SSTSP framework is capable of capturing these oscillations. Figure 11 shows Hovmoeller diagrams of cloud top temperature for SSTSP12, SSTSP22 and SSTSP32 simulations, with the CRM simulation also included for the reference. The figure shows that the variability in SP simulations is of similar character to that in the CRM simulation. However, the zigzag pattern formed by very cold tops of convective cloud systems propagating toward and then away from the convergence region apparent in the CRM simulation is less coherent in the SP model. The coherency decreases with the increase of spatial compression and temporal acceleration. Less coherent propagation of convective systems (in comparison to the CRM simulation) happens even for the SP simulations with no spatial compression and temporal acceleration (not shown). This is consistent with the fact that coherent propagation of convective-scale features across the SP model grid is more difficult than in the CRM model because cloud-scale models communicate only through the large-scale model dynamics. Another feature apparent in Fig. 11 is that convection seems to be more localized in the center of the domain as already documented in Figs. 10 to 11.

c. Low-frequency variability

Low-frequency variability in the CRM simulation has been analysed in detail in SPMG. There, we apply the Empirical Orthogonal Function (EOF) analysis and develop an index of the low-frequency variability. Subsequently, we construct composite of low-frequency variability with lag-regression analysis applying the index. We analyse reconstructed fields of different dynamical variables and describe the low-frequency oscillation. We find low-frequency variability of 20 days period, triggered by anomalously intense deep convection over warm pool. This, in turn, is the consequence of large-scale horizontal advection of anomalously moist air from the subsidence region after the period of moisture buildup through anomalously intense shallow convection.

Here, we investigate if the low-frequency variability is captured applying the SSTSP framework by applying the same methodology as for the CRM simulation in SPMG. First, we perform EOF analysis for the last 290 days of large-scale surface wind data with 1-hour temporal resolution. Subsequently, for every SSTSP simulation, we analyze the low-frequency variability applying the principal component of the leading EOF (see section 4 in SPMG). Table 2 presents main characteristics of the leading EOF for various SSTSP simulations and for the CRM simulations from SPMG. All SSTSP simulations exhibit a dominant mode of low-frequency variability corresponding to a strengthening/weakening of the low level flow as identified previously for the CRM simulation in SPMG. Power spectrum peaks for the period in between 23-26 days and compares reasonably well with the 20-day period of the CRM simulation. It thus appears that SSTSP framework captures the variability corresponding to intra-seasonal frequency band, with the variability responsible for a significant percent of the total variance as in the CRM simulation. Overall, SSTSP simulations with larger spatial compression or temporal acceleration tend to exhibit lower total variance. SSTSP23 and SSTSP24 simulations feature the closest variance to the CRM simulation.

In order to characterize low-frequency oscillation in more detail, composites of low-frequency variability were constructed by regressing various variables on the leading EOF principal component as described in SPMG. All SSTSP simulations reproduce phases of the low-frequency oscillation, with the exemplary composite of the horizontal velocity for SSTSP22 simulation shown in Figs. 12 and 13. Fig. 12 can be compared to Fig. 8 in SPMG, whereas Fig. 15 can be compared to panels (a) in Figs. 9 to 12 in SPMG. As in SPMG, the low-frequency oscillation consists of 4 phases, namely suppressed, strengthening, active and decaying. The mechanism behind low-frequency oscillation is robust and it is reproduced in all SSTSP simulations. As in the CRM simulation, large-scale advection of moisture is correlated with oscillations of convective activity and large-scale circulation. Suppressed phase is characterized by weak large-scale overturning circulation and decreasing deep convective activity in the central part of the domain. This, in turn, is associated with drier troposphere due to anomalously strong mid-tropospheric advection of dry air from the subsidence region and anomalously weak advection of moist surface air to the central part of the domain. At the same time, anomalously weak subsidence allows for moisture buildup over the subsidence region, as shallow convective activity intensifies. Circulation strengthens as low-tropospheric anomalously-moist air is advected to the central part of the domain and deep convection intensifies. As deep convective activity reaches its peak, troposphere warms and dries due to the latent heat release and intense precipitation. The decaying phase follows when the central region dries out because of the intense precipitation, and it is accompanied by a strong mid-tropospheric jet bringing dry air from the subsidence region and advection of anomalously dry low-tropospheric air as shallow convection weakens due to strong subsidence.

4. Discussion and conclusions

The primary purpose of this paper is to evaluate sparse space-time superparameterization (SSTSP) introduced in Xing et al. (2009). SSTSP extends the original superparameterization (SP) approach, where convective processes are simulated explicitly by a cloud-resolving model embedded in every large-scale model column. The motivation behind SSTSP comes from the quest for computationally effordable and statistically accurate simulations of large-scale scale circulations that crucially depend on convective activity. SSTSP addresses this issue by significantly reducing cloud-resolving calculations and at the same time assuring its statistically accurate small-scale (convective) feedback. The feedback is obtained by rescaling statistics from cloud-resolving calcuations over time- and horizontal-domain spans that are reduced relatively to the large-scale time and space resolutions.

Xing et al. (2009) perfomed initial tests of the SSTSP methodology. They conducted idealized simulations of a squall line within 1000-km horizontal domain for a 6-hour period. It was shown that SSTSP captures propagation of a squall line across the domain, with the propagation speed controlled by the prescribed shear. Here, we evaluate SSTSP framework for idealized Walker cell setup. This is a more complex case than in Xing et al. (2009) because it features a wider range of spatio-temporal scales, up to planetary scales and time periods up to several tens of days. In contrast to Xing et al. (2009), larger-scale flow can evolve in response to feedbacks from moist convection, and in turn it can affect subsequent convective development. We evaluate the performance of the SSTSP algorithm by comparing solutions to those obtained applying the cloud-resolving model (CRM) described in Slawinska et al. (2013; SPMG).

We find that SSTSP is capable in reproducing key characteristics of the cloud-resolving Walker cell simulation. In agreement with CRM results, the mean state features the first and second baroclinic modes with deep convection over high SST organized into propagating systems. The properties of these convective systems (e.g., structure, propagation) are affected by the horizontal extent of SP cloud-resolving domains. This is an artifact of the periodicity of embedded cloud-resolving models that cannot be avoided. SSTSP captures intra-seasonal variability predicted by the CRM model that consists of 4 distinctive stages - suppressed, intensification, active and weakening phase - along with the mechanisms driving them. Differences in convective evolution and propagation result in some differences between SSTSP and CRM simulations, such as in the mean sounding, spatial distribution of the cloudiness and surface precipitation, or in the spatio-temporal characteristics of the low-frequency oscillation. Differences in the mean cloudiness (cf. Fig. 9) will most likely be accentuated when interactive radiation transfer scheme is used, an aspect not addressed in the current study.

Numerical simulations discussed here can be put in the context of those discussed in Grabowski (2001; G01 hereafter). Section 3 of G01 presented SP simulations of a 2D flow driven by large-scale SST gradients, although of a significantly smaller horizontal extent (computational domain of 4,000 km in G01 rather than 40,000 km here and in SPMG). SP simulations in section 3 of G01 were compared to CRM simulations discussed in Grabowski et al. (2000). G01's SP simulations used various horizontal gridlengths of the large-scale model (from 20 to 500 km; referred to as P20 and P500, respectively) with the horizontal extent of the embedded periodic-horizontal-domain CRM model matching the large-scale model gridlength. G01 results documented a significant impact of the specific setup of the SP model configuration (i.e., from P20 to P500), especially for the mesoscale convective organization (cf. Fig. 8 therein). In contrast, SP simulations presented here feature just a single 48-km horizontal gridlength of the large-scale model and explore the impact of SSTSP methodology. Such a gridlength can be argued to follow a recommendation of Grabowski (2006a) who suggested that the SP approach is better suited for large-scale models with horizontal gridlengths in the mesoscale range (i.e., a few tens of km). This is because, in the mesoscale gridlength case, the embedded SP models represent effects of small-scale convective motions only, and the convective mesoscale organization (e.g., into squall lines) can be simulated by the large-scale model. Both convective and mesoscale circulations have to be represented by the SP model when the large-scale model gridlength is hundreds of km, as in typical global climate applications (e.g., Khairoutdinov et al. 2005, DeMott et al. 2007, among others). Section 4 of G01 applies the SP methodology to the problem of large-scale convective organization on an idealized constant-SST (”tropics everywhere”) aquaplanet. Although not emphasized there, the SP aquaplanet simulations (as well as subsequent studies, e.g., Grabowski 2006b) already apply the spatial compression methodology because of the disparity between large-scale model gridlength and the horizontal domain size of the embedded CRM model.

The obvious main drawback of the SP approach is that every cloud-resolving model is independent of each other and communicating solely by the large-scale model dynamics (i.e., through the large-scale forcings). The key point is that cloud systems cannot propagate directly from one large-scale gridbox to the other, but they remain locked in a single large-scale gridbox because of the periodic lateral boundary conditions. As discussed by Jung and Arakawa (2005), periodic lateral boundary conditions require the mean mass flux to vanish. As a result, updrafts get weaker as the horizontal extent of the cloud-resolving domain decreases. Large-scale thermodynamical fields are also modified, for instance, the lower/upper troposphere becomes moister/drier. This key drawback of the SP (and thus SSTSP) approach was also noted in other studies (e.g., G01) and it is evident in our simulations.

To overcome these limitations, Jung and Arakawa (2005) suggest an alternative approach where periodic boundary conditions are abandoned and the adjacent cloud-resolving models are linked allowing propagation of small-scale perturbations from one large-scale model gridbox to another. Such an approach is relatively straightforward in a 2D large-scale model framework, but it requires more complicated parallel-processing methods as opposed to "embarassingly parallel" logic of the original SP. Perhaps more importantly, this simple idea leads to a significantly more complex methodology when implemented into a 3D large-scale model (cf. Jung and Arakawa 2010). Considering these factors, we feel that the traditional SP/SSTSP methodology can still serve as a valuable technique in large-scale models featuring mesoscale horizontal gridlengths and variable orientation of SP cloud-resolving models (cf. Grabowski 2004). We hope to report on such numerical experiments in forthcoming publications.

5. References

DeMott, C. A., D. A. Randall, and M. Khairoutdinov, 2007: Convective precipitation variability as a tool for general circulation model analysis. J. Climate., 20, 91112.

Grabowski, W. W., and P. K. Smolarkiewicz, 1999: CRCP: A cloud resolving convection parameterization for modeling the tropical convecting atmosphere. Physica D, 133, 171-178.

Grabowski, W. W., J.-I. Yano, and . W. Moncrieff, 2000: Cloud Resolving Modeling of Tropical Circulations Driven by Large-Scale SST Gradients. J. Atmos. Sci., 57, 20222040.

Grabowski, W. W., 2001: Coupling cloud processes with the large-scale dynamics using the Cloud-Resolving Convection Parameterization (CRCP). J. Atmos. Sci., 58, 978997.

Grabowski, W. W., 2004: An improved framework for superparameterization. J. Atmos. Sci., 61, 1940-1952.

Grabowski. W. W., 2006a: Comments on Preliminary Tests of Multiscale Modeling with a Two-Dimensional Framework: Sensitivity to Coupling Methods. Monthly Weather Review 134:7, 2021-2026

Grabowski, W. W., 2006b: Impact of explicit atmosphere-ocean coupling on MJO-like coherent structures in idealized aquaplanet simulations. J. Atmos. Sci., 63, 2289-2306.

Jung, J.-H., and A. Arakawa, 2005: Preliminary tests of multiscale modeling with a two-dimensional framework: Sensitivity to coupling methods. Mon. Wea. Rev., 133, 649662.

Jung, J.-H., and A. Arakawa, 2010: Development of a quasi-3D multiscale modeling framework: motivation, basic algorithm and preliminary results. J. Adv. Moldel. Earth Syst., 2, DOI:10.3894/JAMES.2010.2.11.

Khairoutdinov, M. F., and D.A. Randall, 2003: Cloud-resolving modeling of the ARM summer 1997 IOP: Model formulation, results, uncertainties and sensitivities. J. Atmos. Sci., 60, 607-625

Khairoutdinov, M.F., D.A. Randall, and C. DeMotte, 2005: Simulations of the atmospheric general circulation using a cloud-resolving model as a super-parameterization of physical processes. J. Atmos. Sci., 62, 2136-2154.

Kuang, Z., P. N. Blossey, and C. S. Bretherton, 2005: A new approach for 3D cloud resolving simulations of large scale atmospheric circulation, Geophys. Res. Lett., 32, L02809, doi: 10.1029/2004GL021024.

Lin, Jia-Lin, and Coauthors, 2006: Tropical Intraseasonal Variability in 14 IPCC AR4 Climate Models. Part I: Convective Signals. J. Climate, 19, 26652690.

Luo, Z., and G. L. Stephens (2006), An enhanced convection?wind? evaporation feedback in a superparameterization GCM (SP?GCM) depiction of the Asian summer monsoon, Geophys. Res. Lett., 33, L06707, doi:10.1029/2005GL025060.

Maloney, E. D., and D. L. Hartmann, 2001: The sensitivity of intraseasonal variability in the NCAR CCM3 to changes in convective parameterization. J. Climate , 14 , 2015-2034.

Slawinska, J., Pauluis, O., A. J. Majda, and W. W. Grabowski, 2014: Multi-scale interactions in an idealized Walker circulation: Mean circulation and intra-seasonal variability. 71, 953-971.

Slingo, J. M., and Coauthors. 1996: Intraseasonal oscillations in 15 atmospheric general circulation models: Results from an AMIP diagnostic subproject. Climate Dyn., 12, 325357.

Smolarkiewicz, P. K., and L. G. Margolin, 1997: On forward-in-time differencing for fluids: An Eulerian/semi-Lagrangian nonhydrostatic model for stratified flows. Atmos.-Ocean, 35, 127-152.

Smolarkiewicz, P. K., 2006: Multidimensional positive definite advection transport algorithm: an overview. Int. J. Numer. Meth. Fluids, 50, 11231144. doi: 10.1002/fld.1071

Soong S. T. and Y. Ogura, 1980: Response of tradewind cumuli to large-scale processes. J Atmos Sci., 37, 20352050.

Soong S. T. and W. K. Tao, 1980: Response of deep tropical cumulus clouds to mesoscale processes. J Atmos Sci 37, 2016-2034.

Tao, W. K., and S. T. Soong, 1986: A study of the response of deep tropical clouds to mesoscale processes: Three-dimensional numerical experiments. J . Atmos. Sci., 43, 2653-2676.

Wheeler, M., and G.N. Kiladis, 1999: Convectively coupled equatorial waves: Analysis of clouds and temperature in the wavenumber-frequency domain. J. Atmos. Sci., 56, 374-399.

Xing, Y., A. J. Majda, and W. W. Grabowski, 2009: New efficient sparse space-time algorithms for superparameterization on mesoscales. Mon. Wea. Rev., 137, 4307-4324.

List of Tables

TABLE 1. Mean precipitable water content (prw; in kg m^{-2})), cloud top temperature (cltop; in K) and precipitation (precip; in mm hr^{-1}).

p_x p_t	prw	cltop	precip
11	53.8	297.3	0.128
12	54.2	294.4	0.130
13	54.6	291.9	0.133
14	54.8	290.0	0.133
21	51.0	297.3	0.122
22	51.1	294.5	0.123
23	51.4	292.4	0.125
24	51.1	290.5	0.125
31	47.0	297.5	0.108
32	47.2	295.2	0.110
33	47.3	293.0	0.111
34	47.6	291.3	0.111
CRM	55.9	296.5	0.157

TABLE 2. Eigenvalue periods of the first EOF for the surface wind time series and standard deviation of its principal component. Simulations with SSTSP algorithm (with p_x and p_t as given in the first column). CRM results are included in the bottom row.

p_x p_t	eigenvalue	period (days)	standard deviation
11	0.51	24	157
12	0.53	26	154
13	0.54	24	159
14	0.42	24	133
21	0.41	26	117
22	0.29	24	85
23	0.39	26	108
24	0.33	26	95
31	0.29	24	86
32	0.22	23	71
33	0.18	23	62
34	0.18	26	63
CRM	0.36	20	88

List of Figures

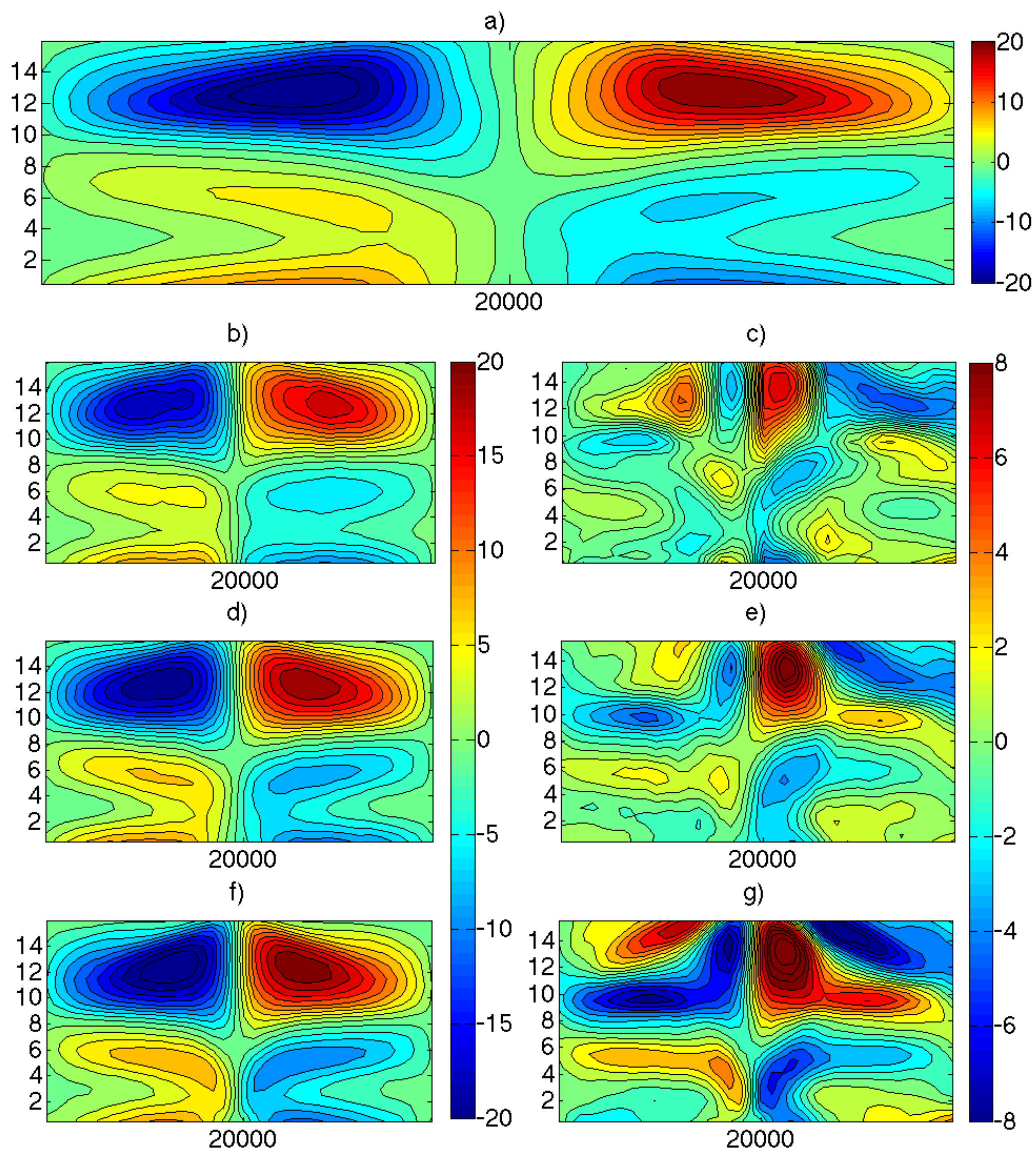

FIG. 1. a) Time averaged horizontal velocity field (m s^{-1}) for CRM. b-g) Time averaged horizontal velocity field (m s^{-1}) for SSTSP11/SSTSP22/SSTSP33 (top/middle/bottom left) simulations and their difference from the CRM simulation (top/middle/bottom right).

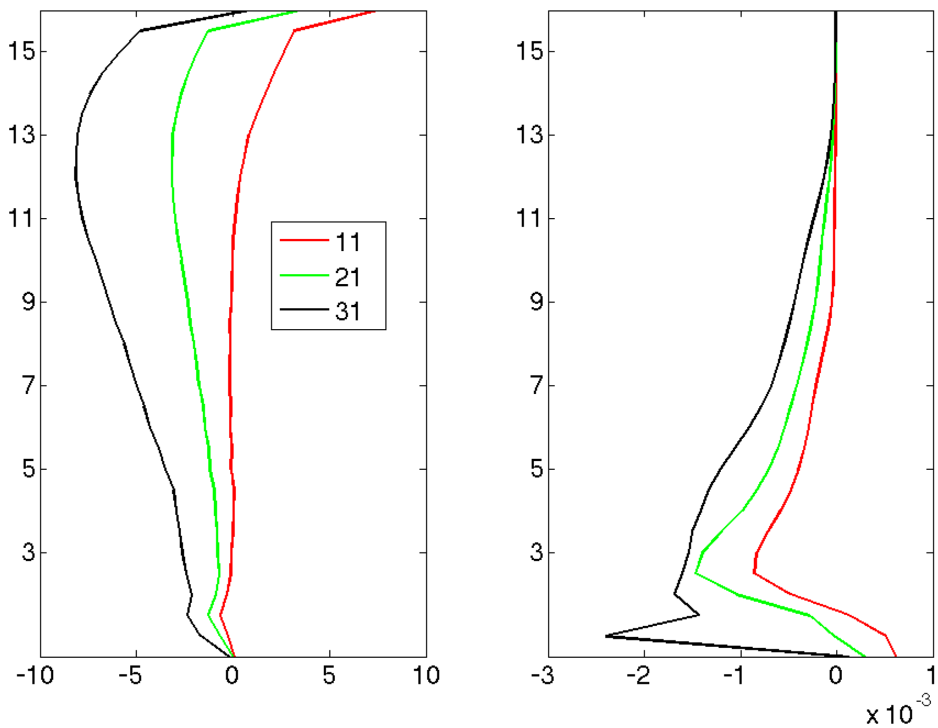

FIG. 2. Difference in the mean profiles of the potential temperature (K, left) and the water vapour mixing ratio (kg kg^{-1}, right) between SSTPS11/SSTSP21/SSTSP31 (red/green/black line) and the CRM simulation.

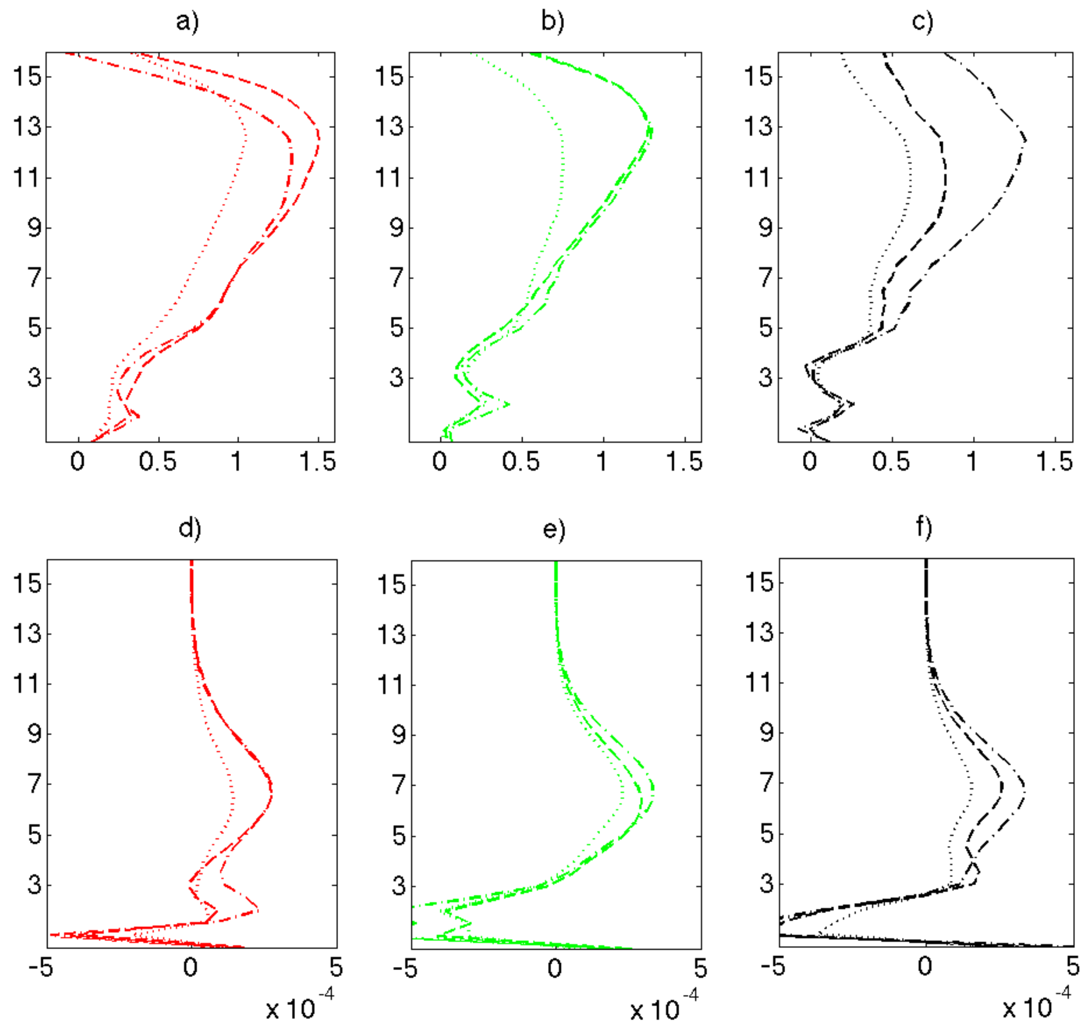

FIG. 3. Difference in mean profiles of the potential temperature (K, top) and the water vapour mixing ratio (kg kg^{-1}, bottom) between SSTSP11/SSTSP21/SSTSP31 (left/middle/right) and SSTSP simulation with the same spatial acceleration p_x and temporal acceleration p_t=2/3/4 (dotted/dashed/dashed-dotted lines), respectively.

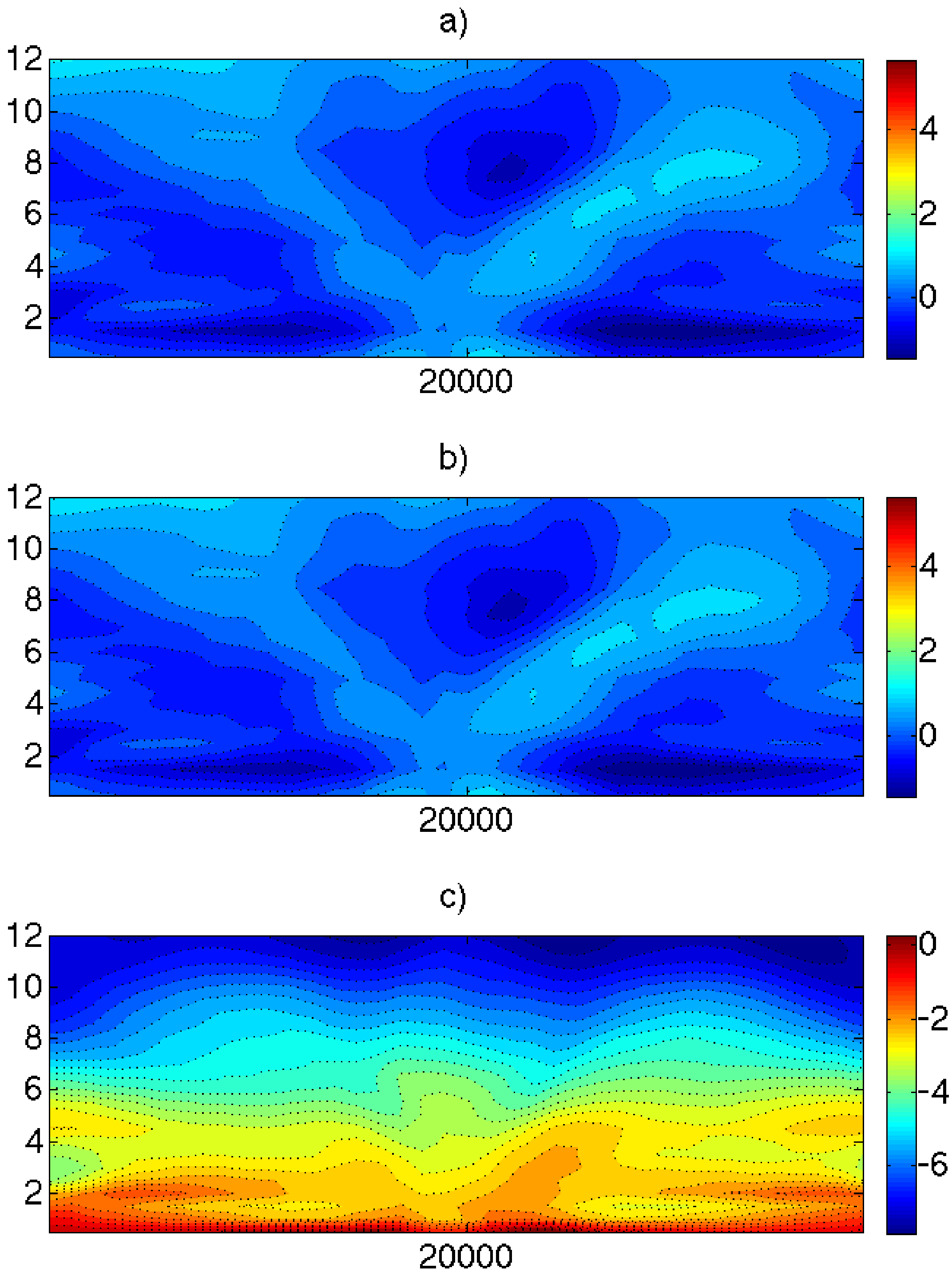

FIG. 4. Spatial distribution of the difference in the time averaged potential temperature field (K) for the SSTSP11/SSTSP22/SSTSP33 (top/middle/bottom) simulation and the CRM simulation.

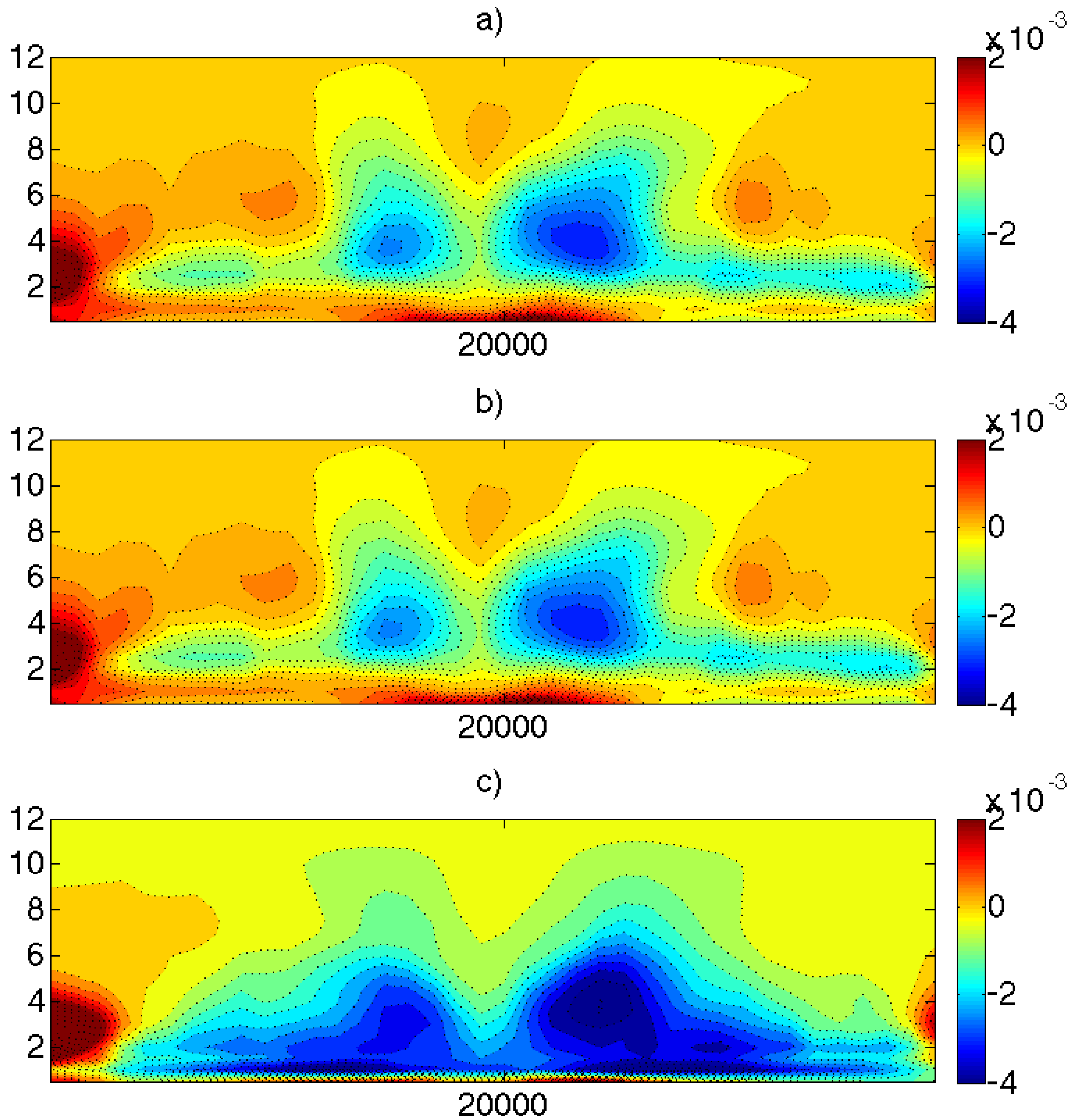

FIG. 5. Spatial distribution of the difference in the time averaged field of the water vapor mixing ratio (kg kg^{-1}) for the SSTSP11/SSTSP22/SSTSP33 (top/middle/bottom) simulation and the CRM simulation.

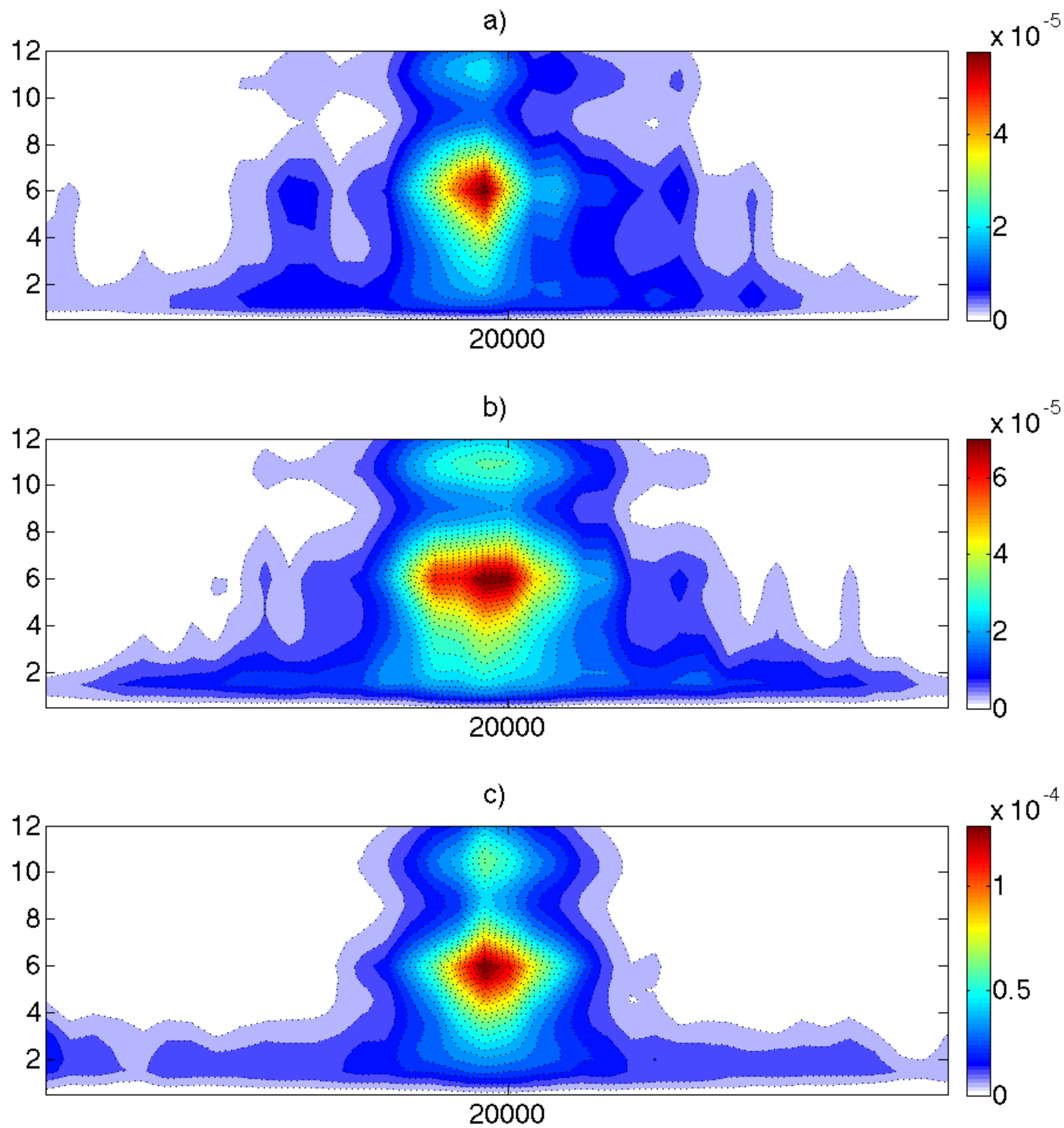

FIG. 6. Spatial distribution of the time averaged cloud water mixing ratio (kg kg^{-1}) for SSTSP11/SSTSP22/SSTSP33 (top/middle/bottom) simulations.

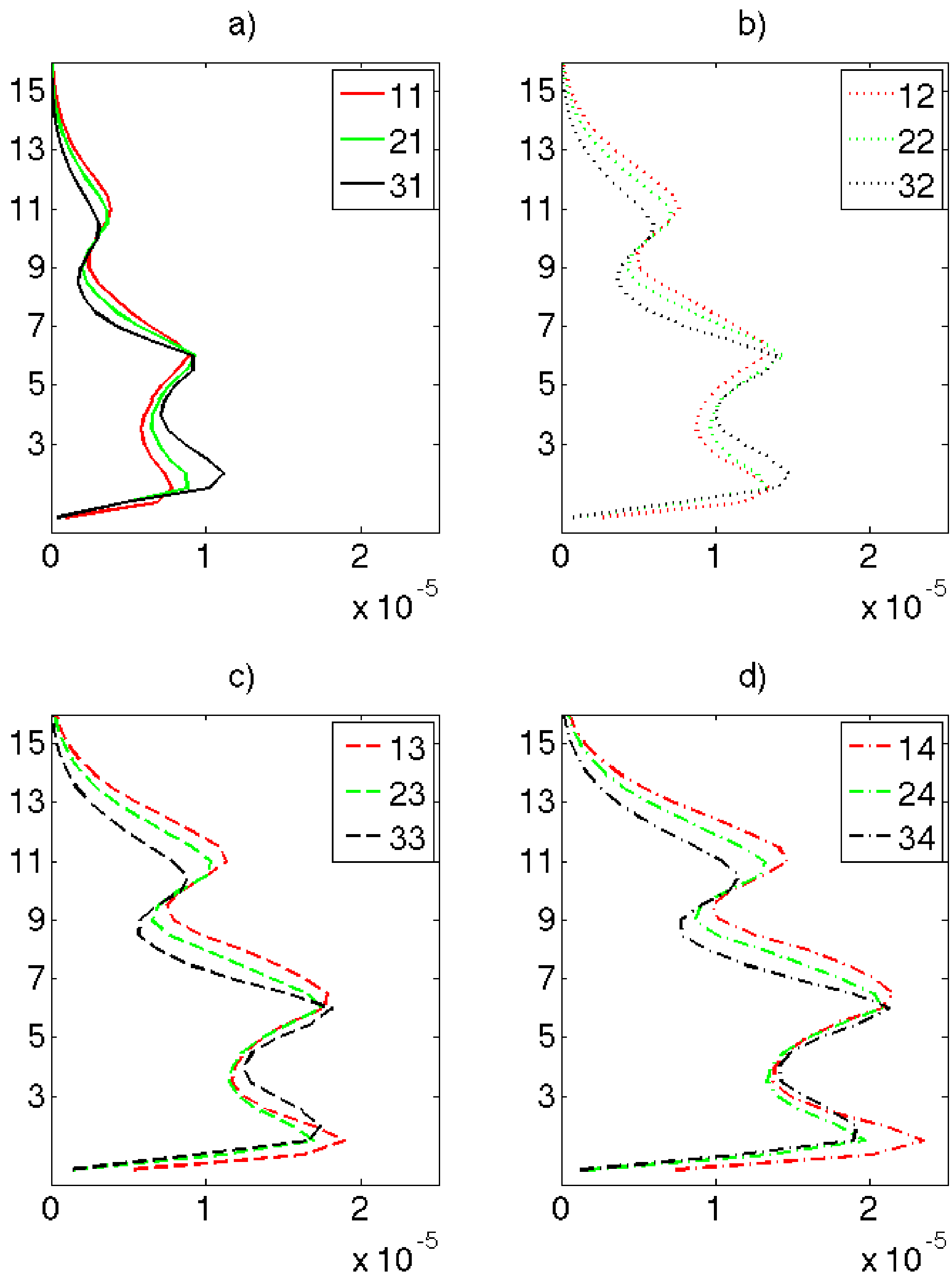

FIG. 7. Mean (time and space averaged) profiles of the cloud water mixing ratio (kg kg^{-1}). Red/green/black lines are for simulations with spatial compression p_x=1/2/3, respectively. Solid/dotted/dashed/dashed-dotted lines are for simulations with temporal acceleration p_t=1/2/3/4, respectively.

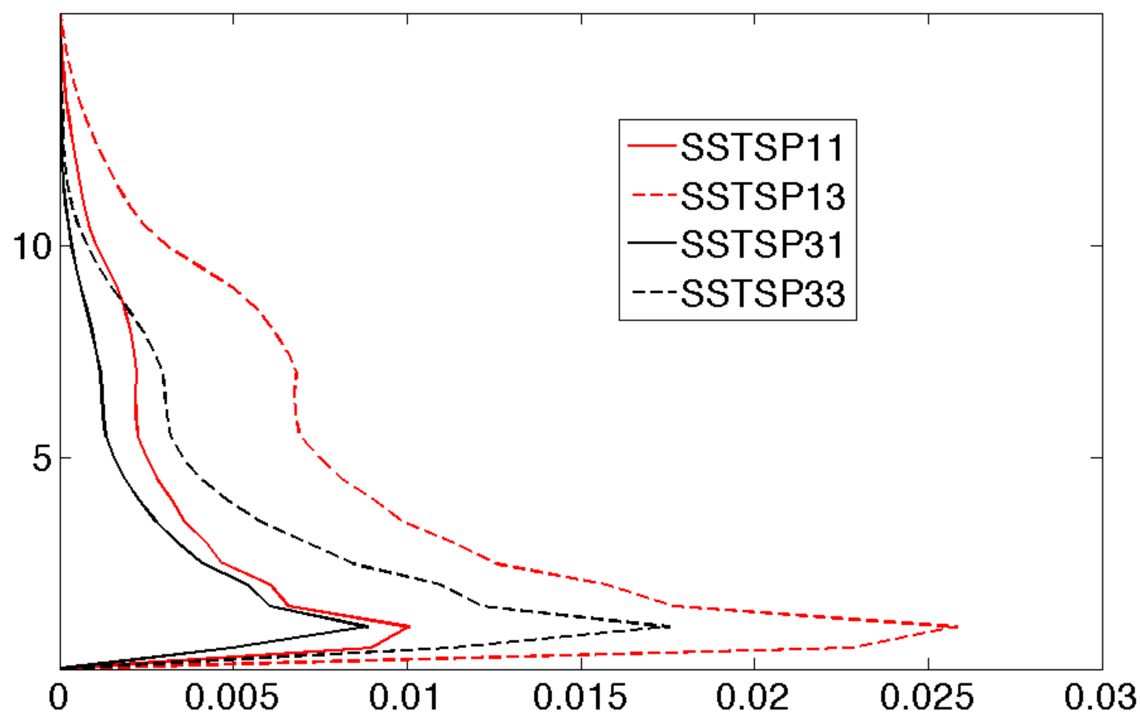

Fig. 8. Mean (time and space averaged) mass flux profiles for simulation with spatial compression 1 or 3 (red or black line) and temporal acceleration 1 or 3 (solid or dashed line).

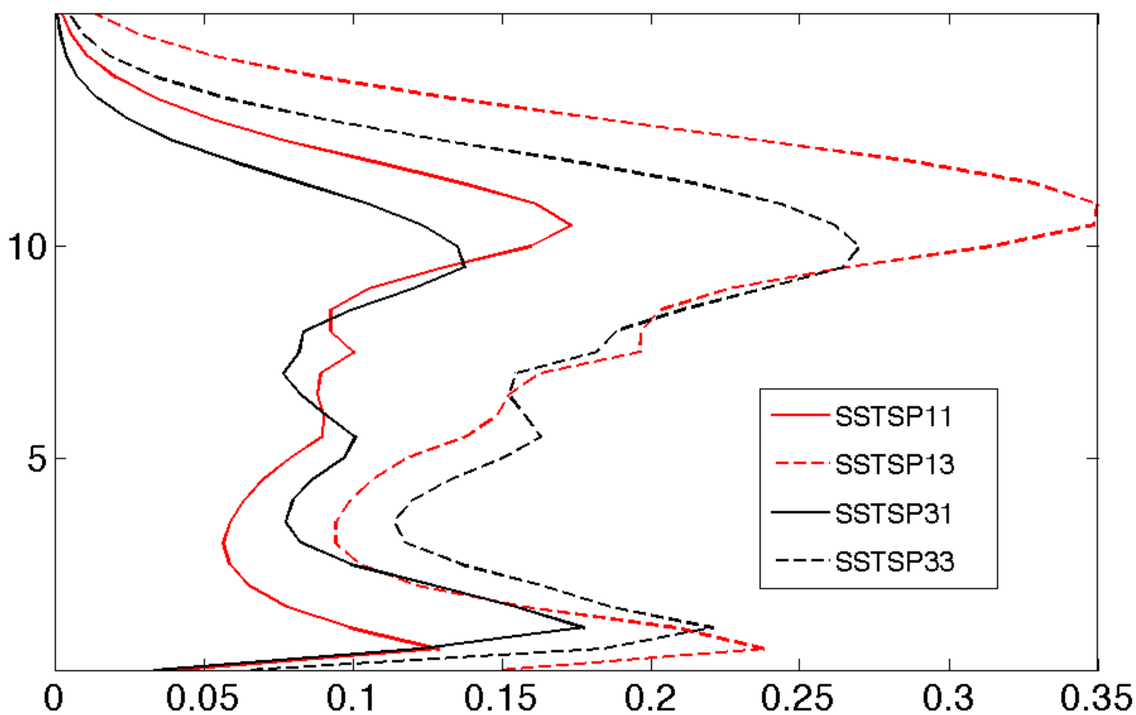

FIG. 9. As Fig. 8, but for the precipitation water water mixing ratio (kg kg[1]).

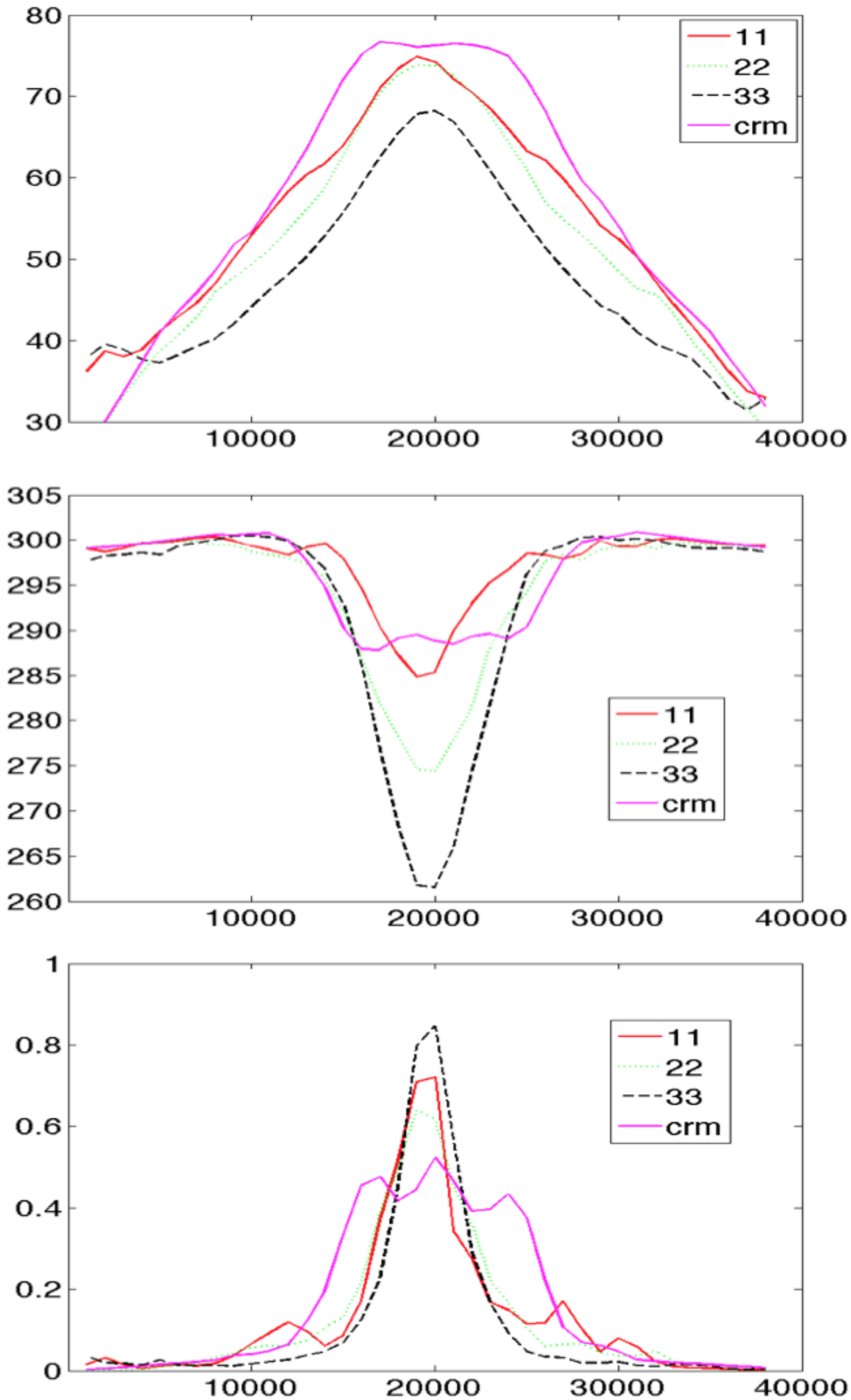

Fig. 10. Time averaged horizontal distribution of precipitable water (kg m^{-2}, top), cloud top temperature (K middle) and precipitation (mmh^{-1}, bottom), for CRM (solid magenda line), SSTSP11 (solid red line), SSTSP22 (dotted green line) and SSTSP33 (dashed black line). Mean values for all simulations are given in Table 1.

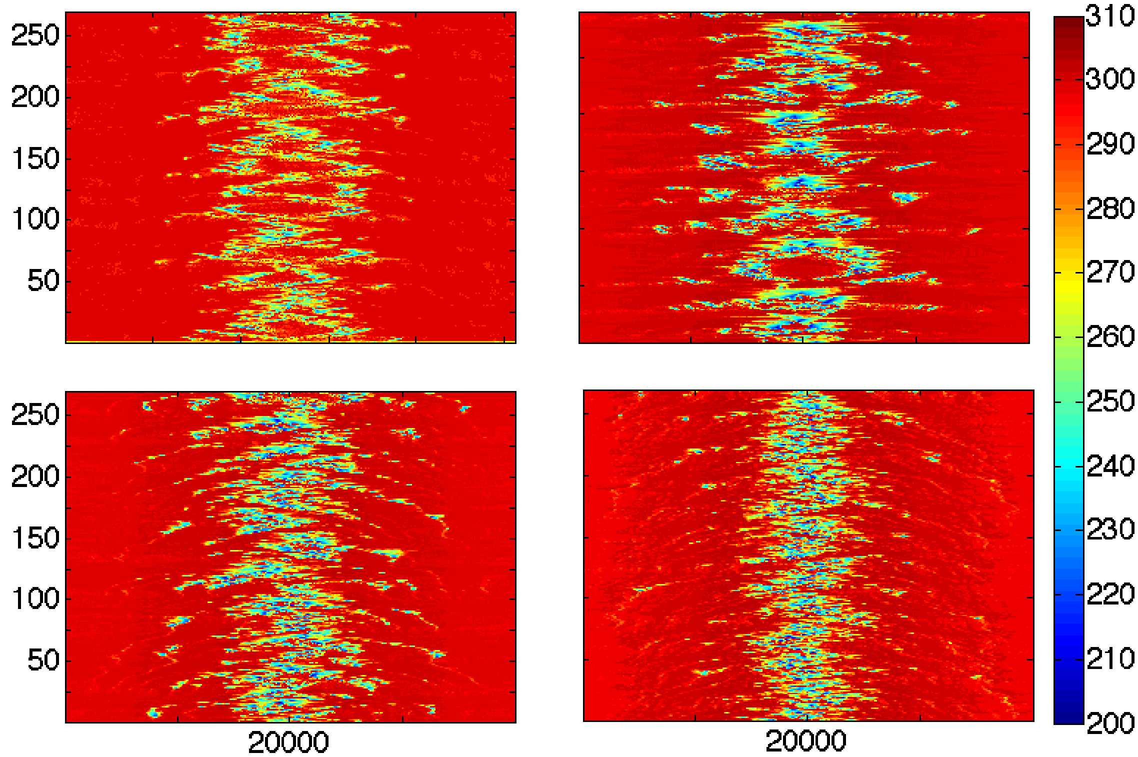

FIG. 11. Hovmoller diagrams of the cloud top temperature for CRM (top left), SSTSP12 (top right), SSTSP22 (bottom left) and SSTSP32 (bottom right) simulations.

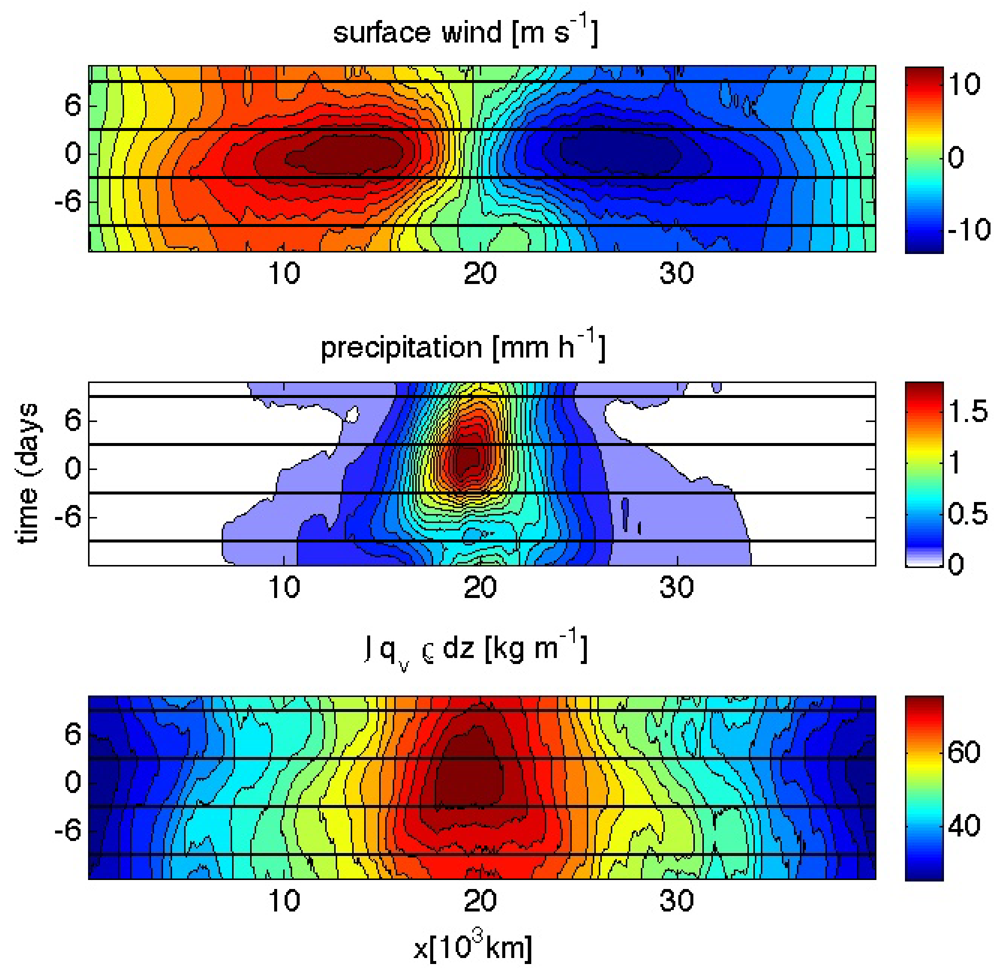

FIG. 12. Hovmoller diagrams of the lag regression of the surface wind (m s^{-1}; upper panel), surface precipitation rate (mm h^{-1}; middle panel)x), and precipitable water (kg m^{-2}; bottom panel) for SSTSP22 simulation.

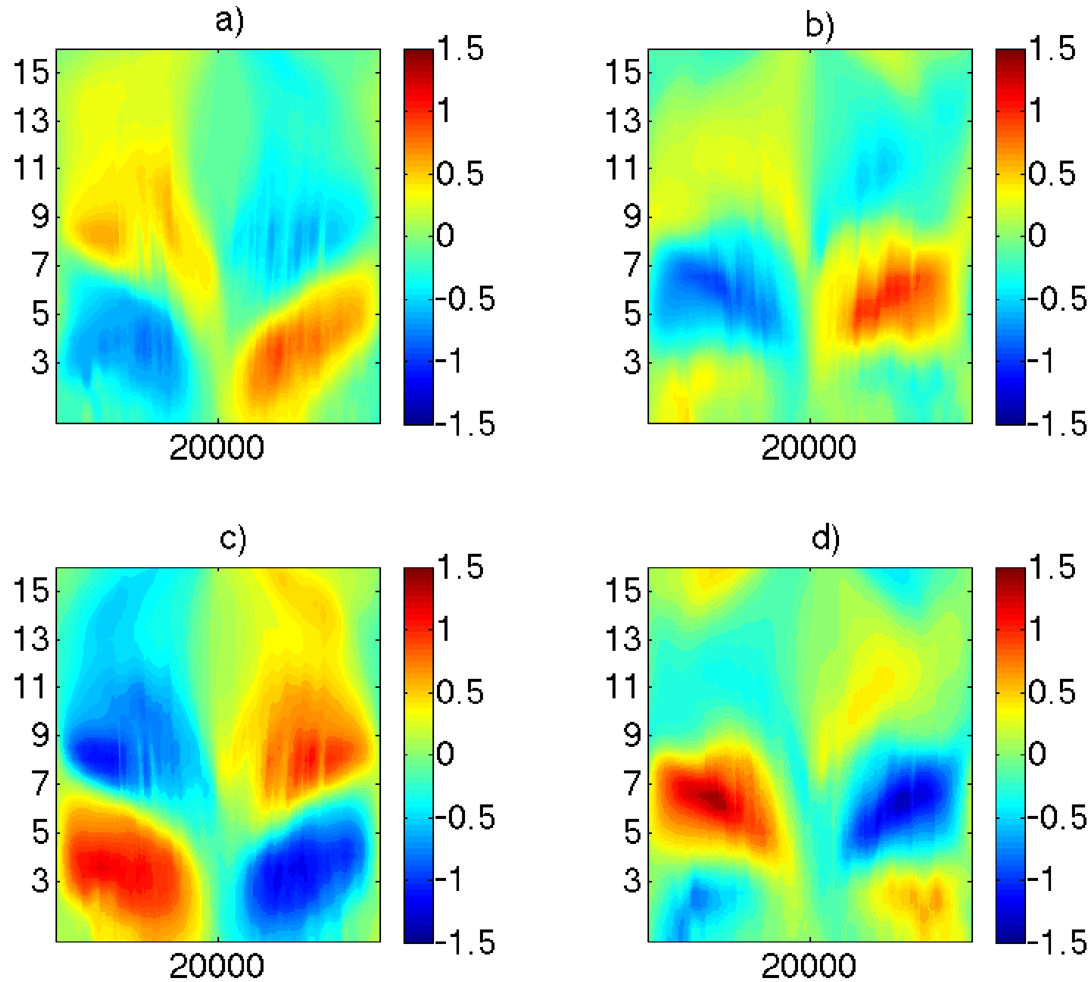

FIG. 13. Lag-regressed structure of the horizontal velocity anomaly for (a) suppressed phase, (b) strengthening phase, (c) active phase, and (d) decaying phase for SSTSP22 simulation.